Higgs mode and stability of *xy*-orbital ordering in Ca_2RuO_4

Guoren Zhang[1] and Eva Pavarini[2,3]
[1]*Key Laboratory of Materials Physics, Institute of Solid State Physics, Chinese Academy of Sciences, Hefei 230031, People's Republic of China*
[2]*Institute for Advanced Simulation, Forschungszentrum Jülich, 52425 Jülich, Germany*
[3]*JARA High-Performance Computing, 52425 Jülich, Germany*

(Received 13 February 2020; accepted 29 April 2020; published 18 May 2020)

We investigate the stability of *xy* orbital ordering and the nature of the magnetic longitudinal excitations in Ca_2RuO_4. To this end, we employ the local-density approximation + dynamical mean-field theory approach, in combination with many-body perturbation theory. We show that the crossover to a nonperturbative spin-orbit regime—-in which *xy*-like orbital ordering is to a large extent quenched—only takes place when the crystal field is sizably reduced with respect to its actual value in Ca_2RuO_4. In the small crystal-field splitting limit, the spin-orbit interaction favors the metal-to-insulator transition. We find that the effects of the spin-orbit interaction remain perturbative even for the less distorted $Ca_{2-x}Sr_xRuO_4$ with $0 < x < 0.2$ (*S-Pbca* phase) and for the S^* phase. We show that, nevertheless, a Higgs mode at $\omega \sim 50$ meV is compatible with *xy*-like orbital ordering in Ca_2RuO_4.

DOI: 10.1103/PhysRevB.101.205128

I. INTRODUCTION

The spin-wave spectra of the Mott insulator Ca_2RuO_4 have been recently measured by several groups using the inelastic neutron scattering technique [1–3]. The interpretation of the experimental data remains controversial, however. Although consensus accumulates that magnetic excitations can be described by a phenomenological effective $S = 1$ Heisenberg-like model with anisotropic terms [1–9], the character of the effective spins, the microscopic origin of their interactions, and the actual nature of the magnetic excitations are still debated.

Magnetism in Ca_2RuO_4 was at first discussed in terms of the Ru^{4+} local-moment picture, i.e., in the weak spin-orbit coupling limit, although with sizably reduced local magnetic moments [10–14]; such local moments originate from the t_{2g}^4 electronic configuration, since e_g states are well separated via the cubic crystal field. Later, an alternative scenario was proposed in which the spin-orbit interaction is key [15,16]. In this picture, magnetism is of the Van Vleck type; it stems from the t_{2g}^4 spin-orbit ground state, which has total angular momentum $J_{\rm tot} = 0$. This Van Vleck scenario is, however, difficult to conciliate with recent findings. One of the signatures of the $J_{\rm tot} = 0$ ground state is the equal occupation of the three t_{2g} orbitals [17]. Theoretically, however, *xy*-like orbital ordering was obtained via the local-density approximation + dynamical mean-field theory (LDA + DMFT) approach [5], even in the presence of spin-orbit interaction [6,7]; the associated electronic configuration is approximately $xy^2xz^1yz^1$, which is at odds with a $J_{\rm tot} = 0$ ground state. This conclusion is supported, besides other experiments [14,18–20], by recent angle-resolved photoemission spectroscopy measurements [21], which show excellent agreement with LDA + DMFT calculations.

Even though it is likely that the $J_{\rm tot} = 0$ scenario does not apply, the hypothesis of excitonic behavior, on the other hand, remains popular for the description of spin waves [3,4,8,9,22] in Ca_2RuO_4. This is in particular due to the recently reported [3] putative Higgs-like mode, found via inelastic neutron-scattering at $\omega \sim 50$ meV. Other neutron-scattering experiments, on the other hand, did not succeed in detecting such a signal [2]; instead, they reported a longitudinal mode at $\omega \sim 30$ meV in $Ca_2Ru_{0.99}Ti_{0.01}O_4$, ascribed to two-magnon excitations. To further complicate the discussion, theoretical results [2,6,7] show that the transverse pseudo-Goldstone modes, detected in all neutron-scattering experiments, can be well described within the *xy*-like orbital-ordering scenario—-treating the spin-orbit interaction as a perturbation. The correct theoretical picture, however, ultimately relies on the stability of *xy*-like orbital-ordering with respect to small lattice distortions and the size of the associated crystal-field splitting. Furthermore, even if *xy*-like orbital ordering is very robust, it has not been fully clarified if it is or isn't compatible with a Higgs-like mode at $\omega \sim 50$ meV.

In the present paper, we address these questions. We find that the reduction in crystal-field splitting necessary to substantially quench *xy*-like orbital ordering (and thus enter the nonperturbative spin-orbit regime) is large. A crossover does take place when the crystal-field splitting is reduced to about half the original value, everything else staying the same. Inside this nonperturbative regime, the spin-orbit interaction favors the metal-insulator transition, differently than in the very large crystal-field limit [6]. For Ca_2RuO_4 itself, we thus confirm that the effects of the spin-orbit coupling can be accounted for by treating the spin-orbit interaction in many-body perturbation theory. We find that, in addition, spin-orbit effects remain perturbative even in the case of the much less distorted $Ca_{2-x}Sr_xRuO_4$ with $0 < x < 0.2$ (*S-Pbca* phase [14]) and in the so-called S^* phase, recently identified

in a current-stabilized semimetallic state [23]. We show that, nevertheless, xy-like orbital ordering is compatible with $\omega \sim 50$ meV Higgs-like modes.

The paper is organized as follows. In Sec. II, we describe in short the model and methods adopted. We use a combination of the LDA + DMFT approach and many-body perturbation theory. The quantum-impurity solver employed in DMFT calculations is the interaction-expansion continuous-time quantum Monte Carlo method, in the implementation of Refs. [5,6]. We calculate spin-wave spectra via a generalized Holstein-Primakoff (HP) transformation and hard-core boson (HCB) approach [24]; the latter includes intrinsic Higgs-like amplitude modes. In Sec. III, we present the results; the conclusions are summarized in Sec. IV. In the Appendices, we provide relevant technical details.

II. MODEL AND METHOD

First we perform LDA + DMFT calculations with and without spin-orbit interaction. To this end, we construct t_{2g} Wannier functions spanning the bands close to the Fermi level, and obtain the associated LDA Hamiltonian, which includes the on-site crystal-field plus spin-orbit term ($i = i'$) and the hopping term ($i \neq i'$),

$$\hat{H}_{\rm LDA} = -\sum_{ii'}\sum_{mm'}\sum_{\sigma\sigma'} t^{i,i'}_{m\sigma,m'\sigma'} c^{\dagger}_{im\sigma} c_{i'm'\sigma'}, \qquad (1)$$

with $m = xy, yz, xz$. A key parameter in this paper is the crystal-field splitting. We define it as the difference $\varepsilon_{\rm CF} = \varepsilon_2 - \varepsilon_1$, where ε_l are the energies of the crystal-field orbitals $|l\rangle_{\rm CF}$, ordered such that $\varepsilon_{l+1} \geqslant \varepsilon_l$. For Ca_2RuO_4, we find from LDA calculations $\varepsilon_{\rm CF} \sim 320$ meV and $\varepsilon_2 \sim \varepsilon_3$. The spin-orbit (SO) interaction enters both in the on-site term and in the hopping integrals; the on-site contribution, dominant, reads

$$\hat{H}_{\rm SO} = \sum_{i\nu}\sum_{m\sigma m'\sigma'} \lambda^{i}_{\nu} \xi^{i\nu}_{m\sigma m'\sigma'} c^{\dagger}_{im\sigma} c_{im'\sigma'}, \qquad (2)$$

where $\xi^{i\nu}_{m\sigma m'\sigma'} = \langle m\sigma | s^{i}_{\nu} l^{i}_{\nu} | m'\sigma'\rangle$ and ν labels the pseudocubic axes; we have previously shown [6] that $\lambda_z \sim \lambda_x \sim \lambda_y = \lambda \sim 106$ meV. We then built the associated generalized three-band Hubbard model, $\hat{H}^{\rm LDA} + \hat{H}^{U}$ with

$$\hat{H}^{U} = \frac{1}{2}\sum_{i}\sum_{mm'pp'}\sum_{\sigma\sigma'} U_{mm'pp'} c^{\dagger}_{im\sigma} c^{\dagger}_{im'\sigma'} c_{ip'\sigma'} c_{ip\sigma}. \qquad (3)$$

The parameters $U_{mm'pp'}$ are elements of the screened Coulomb interaction tensor. The essential terms for t_{2g} electrons are [25] the direct Coulomb interaction, $U_{mm'mm'} = U_{m,m'} = U - 2J(1 - \delta_{m,m'})$, the exchange Coulomb interaction $U_{mm'm'm} = J$, the pair-hopping term, $U_{mmm'm'} = J$, and the spin-flip term $U_{mm'm'm} = J$. We solve the model with dynamical mean-field theory using the interaction-expansion continuous time quantum Monte Carlo impurity solver. More details on the adopted solution method and its implementation can be found in Refs. [5,6]. For the screened Coulomb integrals, we use $U = 2.3$ eV and $J = 0.4$ eV, values obtained via the constrained random-phase approximation approach (cRPA) [26] and established to fit well-known experimental data [6,21]. Based on the LDA + DMFT results in the paramagnetic phase, in the second step we build the associated effective low-energy spin Hamiltonian using many-body perturbation theory. Finally, we construct the spin-wave spectra using two different approaches, the HP method and the hard-core-boson (HCB) method of Ref. [24]. Details on these two methods, in the generalized form relevant for the case of Ca_2RuO_4, can be found in the Appendices.

III. RESULTS

A. Stability of xy-orbital ordering

We have previously shown that in Ca_2RuO_4 the Mott metal-insulator transition is mainly controlled by the change in structure from the *L-Pbca* (long **c** axis) to the *S-Pbca* (short **c** axis) layered perovskite structure [5]. This structural change leads to an increase in the crystal-field splitting $\varepsilon_{\rm CF}$ from ~ 116 meV to ~ 320 meV. For the *S-Pbca* phase, we find orbital occupations quite close to those expected for perfect xy-like orbital ordering [6]; the doubly occupied natural orbital is the lowest energy crystal-field orbital, $|1\rangle_{\rm CF}$, which has a very large overlap with $|xy\rangle$. We have also shown that [6] in the presence of such a large crystal-field splitting, the spin-orbit coupling plays a small role in the actual metal-insulator transition itself or in determining the size of the gap. Adding the spin-orbit interaction even somewhat *reduces* the gap. It also only slightly decreases the orbital polarization, $p = n_{11} - (n_{22} + n_{33})/2$, the order parameter for xy-orbital ordering, to $p \sim 0.9$. Its maximum value, corresponding to full xy orbital ordering, is $p = 1$; for a $J_{\rm tot} = 0$ ground state, instead, one should find $p = 0$. Furthermore, the most occupied orbital remains, even in the presence of spin-orbit coupling, very close to xy; indeed, if we calculate the orbital polarization in the t_{2g} basis, $p_{\rm CF} = n_{xy} - (n_{xz} + n_{yz})/2$, we find $p_{\rm CF} \approx p$.

The question we address here is how stable xy-orbital ordering is under small decrease in the crystal-field splitting, e.g., arising from small reductions in the local static distortions, experimental errors in their estimations, or that can eventually be tuned by chemical or strain [27] engineering. In short, how small should $\varepsilon_{\rm CF}$ be to radically change the picture, making the effects of the spin-orbit interaction nonperturbative and pushing the system toward the $J_{\rm tot} = 0$ ground state? To answer this question, we study the evolution of the electronic property in a series of idealized systems in which the crystal-field splitting $\varepsilon_{\rm CF}$ is progressively reduced [28]. Calculations are performed keeping the type of distortion (i.e., the shape of the crystal-field orbitals) frozen and merely varying the strength of the field. The main results are summarized in Fig. 1, which shows representative calculations for the three emerging regimes: $\varepsilon_{\rm CF} = \varepsilon_{\rm LDA}$, $\varepsilon_{\rm CF} = \varepsilon_{\rm LDA}/2$, and $\varepsilon_{\rm CF} = 0$. Calculations are all performed at $\sim$290 K, i.e., well inside the experimental paramagnetic Mott insulator phase, the phase relevant for the present analysis.

The panels on the left-hand side of Fig. 1 show the diagonal elements $A_{ll}(\omega)$ of the spectral function matrix for the case $\varepsilon_{\rm CF} = \varepsilon_{\rm LDA}$. The spectral functions shown are in the natural orbital basis, $|l\rangle$. For $\varepsilon_{\rm CF} = \varepsilon_{\rm LDA}$, the $|l\rangle$ basis is very close to the crystal-field basis, $|l\rangle_{\rm CF}$. The orbital polarization p is about its maximum value for xy-like orbital ordering ($p = 1$), and $p_{\rm CF} \approx p$. These panels therefore show that the system is in the xy-like orbital ordering regime; there is very little difference between the spectral functions with (bottom) and without

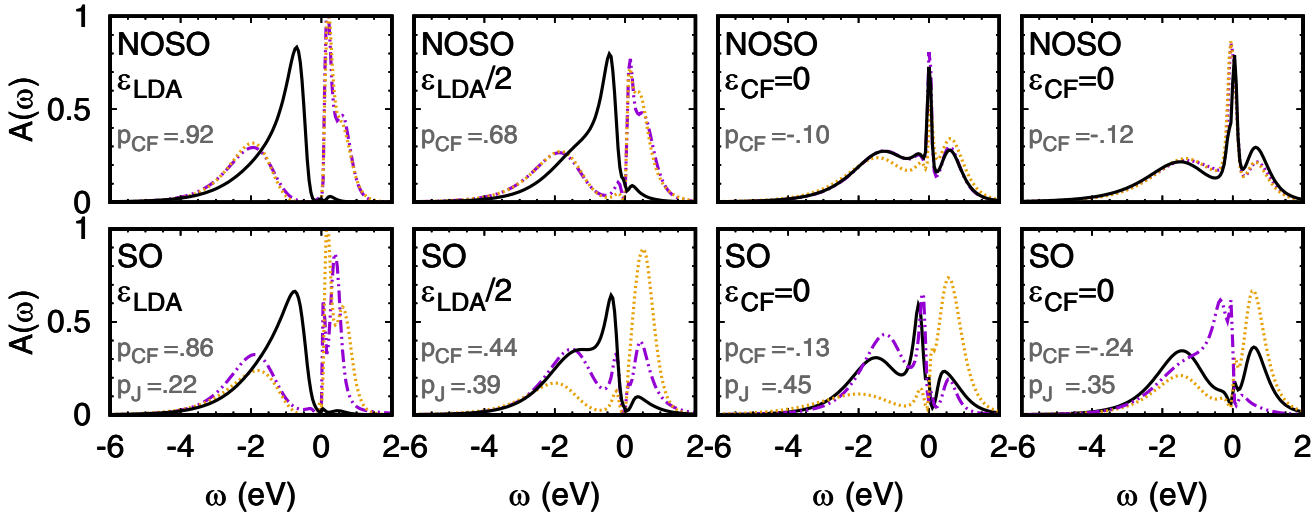

FIG. 1. (Color online.) Orbital-resolved LDA + DMFT t_{2g} spectral function in the basis of natural orbitals for decreasing crystal-field splitting. The energy zero is the chemical potential. Full line: Natural orbital with largest overlap to the ground crystal-field state, $|1_{CF}\rangle$. Dashed and dotted lines: Remaining natural orbitals. Parameters: $U = 2.3$ eV, $J = 0.4$ eV, 290 K. From left to right: $\varepsilon_{CF} = \varepsilon_{LDA}$, $\varepsilon_{CF} = \varepsilon_{LDA}/2$, and $\varepsilon_{CF} = 0$. Last panels on the right: $\varepsilon_{CF} = 0$, density-density approximation for the Coulomb interaction. In each case, we specify $p_{CF} = n_{1_{CF}1_{CF}} - (n_{2_{CF}2_{CF}} + n_{3_{CF}3_{CF}})/2$, the orbital polarization for xy orbital ordering, and $p_J = (n_{3/2}/2 - n_{1/2})/2$, the spin-orbital polarization associated with a $J_{tot} = 0$ state.

(top) spin-orbit interaction, except for a small reduction in the value of p_{CF} and in the size of the gap in the case with finite spin-orbit interaction [6,7].

In the next (going from left to right) panels of Fig. 1, we show the crossover regime. In this case, the crystal-field splitting is one-half the LDA value, $\varepsilon_{CF} = \varepsilon_{LDA}/2 \sim 160$ meV, and thus only 1.5 times larger than the spin-orbit coupling λ. One can see that, in the absence of the spin-orbit interaction (top panel), the system is on the verge of the insulator to metal transition. It remains inside the xy-like orbitally ordered regime, however. The occupations of the natural orbitals are such that $n_2 \sim n_3$; the mostly occupied natural orbital, $|1\rangle$, stays close to the lowest energy crystal-field orbital, $|1_{CF}\rangle \sim |xy\rangle$, with overlap $\langle 1|1_{CF}\rangle \sim 0.94$. The orbital polarization is $p \sim 0.82$; in the crystal-field basis, $p_{CF} \sim 0.68$. If now we switch on the spin-orbit interaction keeping all the rest the same (bottom panel), the situation changes drastically; the most occupied Kramers doublet ($n_1 \sim 1.84$) has approximately the form $|1\rangle_\sigma \sim 0.885|1_{CF}\rangle_\sigma + s_\sigma e^{is_\sigma\phi}(0.325|2_{CF}\rangle_{-\sigma} - is_\sigma 0.307|3_{CF}\rangle_{-\sigma})$; for simplicity, here we dropped the small components. Thus, it still has a large overlap with $|1_{CF}\rangle$, but also with the total angular momentum state $|j, m_j\rangle = |3/2, \pm 1/2\rangle$. In addition, a second Kramers doublet is occupied by 1.4 electrons, $|2\rangle_\sigma \sim |3/2, \pm 3/2\rangle$. The third Kramers doublet has the approximate form $|3\rangle_\sigma \sim -0.431|1_{CF}\rangle_\sigma + s_\sigma e^{is_\sigma\phi'}(0.630|2_{CF}\rangle_{-\sigma} + is_\sigma 0.637|3_{CF}\rangle_{-\sigma})$, approaching the $|1/2, \pm 1/2\rangle$ state, and it is occupied by only $n_3 \sim 0.76$ electrons. The orbital polarization for xy-like orbital ordering is still large, $p \sim 0.76$, but in the crystal-field basis is already half its maximum value $p_{CF} \sim 0.44$. It is useful to calculate the (normalized) order parameter for a $J_{tot} = 0$ ground state, p_J, defined via the equation $p_J = (n_{3/2}/2 - n_{1/2})/2$. This parameter takes the value $p_J = 1$ if the $j = 3/2$ state is fully occupied, and the value $p_J = 0$ if the occupations are all the same ($n_{3/2} = 2n_{1/2}$). For the structure with full LDA crystal-field splitting, we find $p_J \sim 0.22$; when the crystal field splitting is reduced to $\varepsilon_{LDA}/2$ we have instead $p_J \sim 0.39$, less than half its maximum value. The crossover occurs when $p_J \sim p_{CF}$.

Further decreasing the crystal-field splitting to zero yields, in the absence of spin-orbit interaction, a nonpolarized metallic state and, in the presence of spin-orbit interaction, an orbitally polarized bad metal/insulator. In this case, the occupied natural orbitals are close to the four states with total angular momentum $j = 3/2$; more specifically, we obtain the Kramers doublets $|1\rangle_\sigma \sim |3/2, \pm 3/2\rangle$ with $n_1 \sim 1.74$ and $|2\rangle_\sigma \sim |3/2, \pm 1/2\rangle$, with $n_2 \sim 1.54$. This means that we have an inversion of levels with respect to the half-crystal-field case. The figure shows that the xy-like orbital ordering picture completely breaks down, since, although $n_3 \sim 0.71$ is more or less the same obtained in the case $\varepsilon_{CF} = \varepsilon_{LDA}/2$, n_2 is approaching n_1 and $A_{1,1}(\omega) \sim A_{2,2}(\omega)$. This is a signature that the system is now indeed close to an effective $J_{tot} = 0$ ground state. The order parameter $p_J(T)$ increases relatively slowly with temperature, i.e., it is about $p_J \sim 0.19$ at 1200 K and about half its maximum value ($p_J \sim 0.45$) at 290 K; the effect of the spin-orbit coupling is (relatively) quickly suppressed rising the temperature. In addition, the $J_{tot} = 0$ ground state is very sensitive to approximations, e.g., it is already quenched by simply making the density-density approximation for Coulomb terms (right-hand panels of Fig. 1, $p_J = 0.35$), in large part due to the overestimation of the Coulomb-induced spin-orbit anisotropy enhancement in this specific case. In the large crystal-field splitting limit, the same approximation tends to slightly stabilize xy-like orbital ordering with respect to the $J_{tot} = 0$ ground state, although the effect appears weaker (e.g., $\delta p_{CF} = 0.04$ at 290 K).

In conclusion, although the realization of the $J_{tot} = 0$ ground state basically requires zero crystal-field splitting, and temperatures well below the onset of the *S-Pbca* phase,

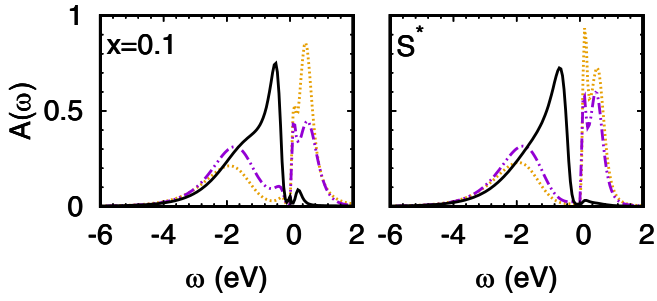

FIG. 2. (Color online.) Orbital-resolved LDA + DMFT t_{2g} spectral function in the basis of natural orbitals (290 K) in *S-Pbca* $Ca_{2-x}Sr_xRuO_4$ (left) and in S^* Ca_2RuO_4 (right). Full line: Natural orbital with largest overlap to the ground crystal-field state, $|1_{CF}\rangle$. Dashed and dotted lines: remaining natural orbitals. Parameters: $U = 2.3$ eV, $J = 0.4$ eV. The energy zero is the chemical potential.

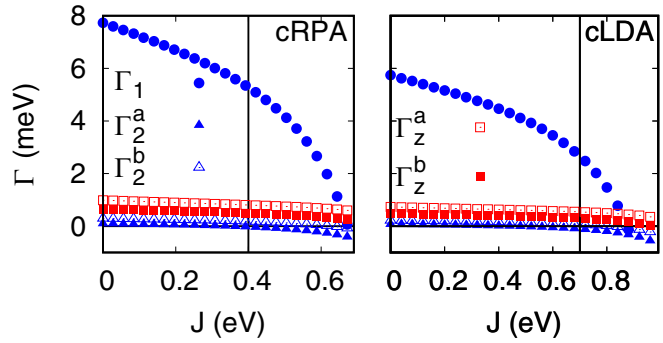

FIG. 3. Exchange parameters as a function of the Hund's rule coupling J. The vertical lines show the cRPA (left panel) and cLDA (right panel) J value. $\Gamma > 0$ if the coupling is antiferromagnetic, $\Gamma < 0$ if it is ferromagnetic.

nonperturbative spin-orbit effects start to appear earlier, when the crystal-field splitting is about half its LDA value. Still, this reduction is large. For Ca_2RuO_4, it is very unlikely that the theoretical crystal-field splitting is overestimated by such a large factor; our LDA + DMFT results describe indeed very well recent angle-resolved photoemission spectroscopy measurements [21].

Based on these results, however, spin-orbit effects could be much more important for $Ca_{2-x}Sr_xRuO_4$ with $x < 0.2$, in the region of the phase diagram where the *S-Pbca* phase persists. Indeed, distortions decrease [14] with increasing x, eventually leading to an insulator-to-metal transition [5], while we have shown [6,7] that the bare spin-orbit couplings are basically the same in Ca_2RuO_4 and Sr_2RuO_4. By adopting the same approach to calculate it, for $x = 0.1$ we do find an LDA crystal-field splitting of about 240 meV, using the structural data reported in Ref. [14], with the lowest energy crystal-field orbital still close to $|xy\rangle$. This is a reduction corresponding to $0.75\,\varepsilon_{CF}$, not so far from the crossover regime. Another interesting candidate could be the S^* phase [23] of Ca_2RuO_4. For this structure, we find an intermediate value, $\varepsilon_{CF} \sim 290$ meV. To explore the possible realization of the nonperturbative spin-orbit regime in these two less distorted systems, we perform additional LDA + DMFT calculations for these compounds. The principal results are shown in Fig. 2. We find that, while the effects of the spin-orbit interaction are indeed somewhat stronger, the changes in structural distortions are, in both systems, still not sufficient to drive the system well inside the nonperturbative regime. In the case of $Ca_{1.9}Sr_{0.1}RuO_4$, the compound which, among those considered here, has the smallest crystal-field splitting, we find $p_J = 0.29$. This value is only slightly larger than in Ca_2RuO_4. Both $Ca_{1.9}Sr_{0.1}RuO_4$ and S^* Ca_2RuO_4 thus remain quite close to xy-like orbital ordering, which proves hard to quench in the insulating phase of the layered ruthenates.

B. Transverse and longitudinal spin-wave modes

The LDA + DMFT results presented so far confirm that the xy-like orbitally ordered picture is very robust in Ca_2RuO_4. It persists when distortions are reduced by partially replacing Ca with Sr and even in the recently identified current-induced modified structure. In light of all this, we thus re-examine the spin-wave spectra. We have previously shown [6] that, in the xy-like orbital-ordering limit, many-body perturbation theory leads to the (minimal) low-energy $S = 1$ model Hamiltonian:

$$\hat{H}_S = \frac{1}{2}\sum_{js\neq j's'} \Gamma_{js,j's'}\mathbf{S}_{js}\cdot\mathbf{S}_{j's'} + \sum_{js\mu\mu'} S_{js;\mu} D_{\mu,\mu'} S_{js;\mu'}. \quad (4)$$

Here, $S_{js;\mu}$ is the μ ($\mu = a, b, c$) component of a spin at site s in the magnetic unit cell j; $\Gamma_{js,j's'}$ is the superexchange coupling between site $i = js$ and $i' = j's'$; only coupling between first and second neighbors are accounted for. $D_{\mu,\mu'}$ is the single-ion anisotropy tensor; in addition to the zero-field term, the spin-orbit interaction yields small anisotropy in the exchange couplings and a small asymmetric exchange interaction, here neglected to keep the model minimal. The low-energy Hamiltonian Eq. (4) gives a very good description of pseudo-Goldstone modes [1,2,6,7]. Next we want to clarify whether, with the same parameters, it can also account well for the highly debated 50 meV longitudinal mode.

Before we proceed, let us discuss the robustness of the theoretical estimates of the couplings in Eq. (4). Using the cRPA values for the screened Coulomb interactions, $(U, J) = (2.3, 0.4)$ eV we find, via second-order perturbation theory in the hopping integrals, the following values for the superexchange coupling: $\Gamma_1 = \Gamma_{i,i+(\mathbf{a}\pm\mathbf{b})/2} \sim 5.3$ meV, next-nearest-neighbor couplings $\Gamma_2^a = \Gamma_{i,i+\mathbf{a}} \sim -0.02$ meV (along $\mathbf{a}$), $\Gamma_2^b = \Gamma_{i,i+\mathbf{b}} \sim 0.18$ meV (along $\mathbf{b}$), and the interlayer couplings $\Gamma_z^a = \Gamma_{i,i+(\mathbf{a}+\mathbf{c})/2} \sim 0.8$ meV, $\Gamma_z^b = \Gamma_{i,i+(\mathbf{b}+\mathbf{c})/2} \sim 0.5$ meV. The interlayer exchange couplings $\Gamma_z^{a/b}$ are sizably larger than $\Gamma_2^{a/b}$, a sign of weak but non-negligible three dimensional magnetism. This result indicates that the so-called A-centered magnetic configuration [12] has lower energy than the B-centered configuration, in line with experiments [2,29]. Neutron-scattering data have in addition shown that a weak Ti doping (∼1%) can reverse the situation, [2] in agreement with the fact that the difference in the two interplane couplings Γ_z^a and Γ_z^b is relatively small. In Fig. 3, we show that these theoretical values are not very sensitive to the (unavoidable) uncertainties in the screened Coulomb interaction couplings (U, J). In the figure, we compare $\Gamma_{i,i'}$ obtained using screened Coulomb integrals calculated via the constrained local-density

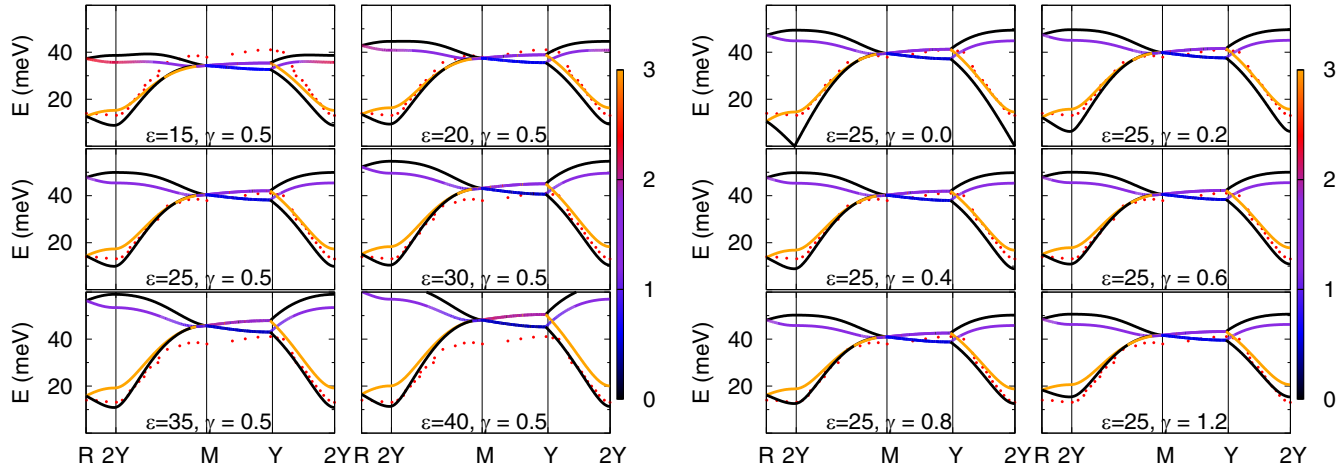

FIG. 4. The magnon dispersion of Ca_2RuO_4 obtained using HP spin-wave theory. Dots: Experimental points corresponding to the maximum of intensity, taken from Fig. 3 in Ref. [1]. Lines: Theory. Ordered magnetic moments along **b** axis: $M^b = 1$. Magnetic configuration: A-centered. Transverse magnetic intensity: $I^a + I^c$. Left panels: Effect of varying ε for constant γ. Right panels: Effect of varying γ for constant ε. Special points: $R = (0, 2\pi, \pi)$, $2Y = (0, 2\pi, 0)$, $M = (\pi, \pi, 0)$, $Y = (0, \pi, 0)$, where all orthorhombic lattice constants are set equal to 1 for simplicity. The mode intensity scale is given on the right of each panel.

approximation [30] (cLDA), $U = 3.1$ eV and $J = 0.7$ eV, and via the cRPA. The exchange couplings change little in a wide range of Hund's rule coupling values. The parameter which varies most with (U, J) is the largest, Γ_1; however, even its variation is small when J stays within a realistic range, in the interval between the cRPA and the cLDA value. The hierarchy of interactions is thus very robust; the obtained values agree well with experimental estimates [1,2].

Let us now turn to the zero-field tensor $D_{\mu,\mu'}$. This is obtained using second-order perturbation theory in the spin-orbit interaction. By diagonalizing $D_{\mu,\mu'}$, we calculate the local axes $\mathbf{a}'$, $\mathbf{b}'$, and $\mathbf{c}'$; in the specific case of Ca_2RuO_4, we find a hard magnetization axis $\sim\mathbf{c}$ and an easy plane is $\sim\mathbf{ab}$. The key elements of the tensor are thus $\varepsilon > 0$ and $\gamma > 0$, where $\gamma = D_{a'a'} - D_{b'b'}$ and $\varepsilon = D_{c'c'} - D_{b'b'}$. The elements of the zero-field tensor increase with the square of the spin-orbit coupling λ. LDA + DMFT calculations yield an effective enhancement [6,31–33] of λ. Recently, this theoretical prediction was confirmed by a high-resolution photoemission experiment in Sr_2RuO_4 [34], the sister compound of Ca_2RuO_4. The effective enhancement has a large Hartree-Fock-like component (corresponding to a factor of 2 or more), which can be taken into account via an effective spin-orbit coupling, $\lambda_{\text{eff}} = \lambda + \Delta\lambda$. The other key factor determining $D_{\mu,\mu'}$ is the specific form of the most occupied natural orbitals in the orbitally ordered state.

Using a relatively moderate isotropic spin-orbit enhancement [6], one finds $\varepsilon \sim 16$ and $\gamma \sim 0.74$ meV; furthermore, with perfect xy-orbital ordering, the easy axis is exactly in the **ab** plane. With a spin-orbit enhancement closer to the value obtained in LDA + DMFT calculations ($\lambda_{\text{eff}} \sim 2\lambda$) and assuming the lowest energy crystal-field orbitals as the doubly occupied state, in line with DMFT results, we have $\varepsilon \sim 25$, with the easy axis slightly tilted [2,8] along **c**. Small elements of the $D_{\mu,\mu'}$ tensor (those $\sim$1 meV or smaller) are of course very sensitive to the precise form of the occupied natural orbital and to (small) experimental uncertainties in lattice distortions. However, we find that the dominant $D_{\mu,\mu'}$ parameters and the hierarchy of interactions (hence the emerging picture) are very robust. The picture does not change qualitatively, for example, if we take into account that the Coulomb interaction also enhances the spin-orbit anisotropy; for Ca_2RuO_4, we find that the latter does not affect much the value of the small parameter γ, while it enhances ε, everything else remaining the same. In conclusion, our calculations show that, in the full range of realistic Coulomb parameters, although the spin-orbit interaction can be treated at a perturbative level, the single-ion anisotropy is large, with the hard axis energy ε larger than the dominant superexchange coupling Γ_1, varying within the range (15,30) meV; the in-plane anisotropy is much smaller, with $\gamma \ll \varepsilon, \Gamma_1$, and it varies in the range (0.5,4) meV.

Let us investigate the spin-wave spectra for single-ion tensor anisotropy parameters in the range discussed above. Starting from the magnetic Hamiltonian Eq. (4), we calculate the spin waves using two approaches. The first is based on the standard HP transformation and the second on HCB spin-wave theory. The latter [24] accounts explicitly for longitudinal amplitude modes. Details on the approaches, generalized to the specific case of Ca_2RuO_4, are given in Appendices. The magnon dispersion depends on the parameters ε, γ, but also on the Fourier transform of the magnetic exchange couplings,

$$\Gamma_{\mathbf{k}}^{s,s'} = \frac{1}{2}\sum_{j>0} \Gamma_{0s;js'} e^{i\mathbf{k}\cdot(\mathbf{R}_{js'} - \mathbf{R}_{0s})},$$

where $\mathbf{R}_{js}$ are Ru position vectors. Its average is $\Gamma_{\mathbf{k}} = -\sum_s \Gamma_{\mathbf{k}}^{1,s}\sigma_1\sigma_s$, where the weights σ_s distinguish the A- and B-magnetic configurations; we find $\Gamma_{\mathbf{0}} \sim 11$ meV for the A configuration and a somewhat smaller value, $\Gamma_{\mathbf{0}} \sim 9.8$ meV, for the B configuration.

The main results are summarized in Fig. 4 (HP spin-wave theory) and in Fig. 5 (HCB spin-wave theory); calculations are compared to the experimental data from Refs. [1–3]. In the limit case $\varepsilon = \gamma = 0$, the HP and the HCB spin-wave theory yield the same transverse modes. For finite ε and γ, the two

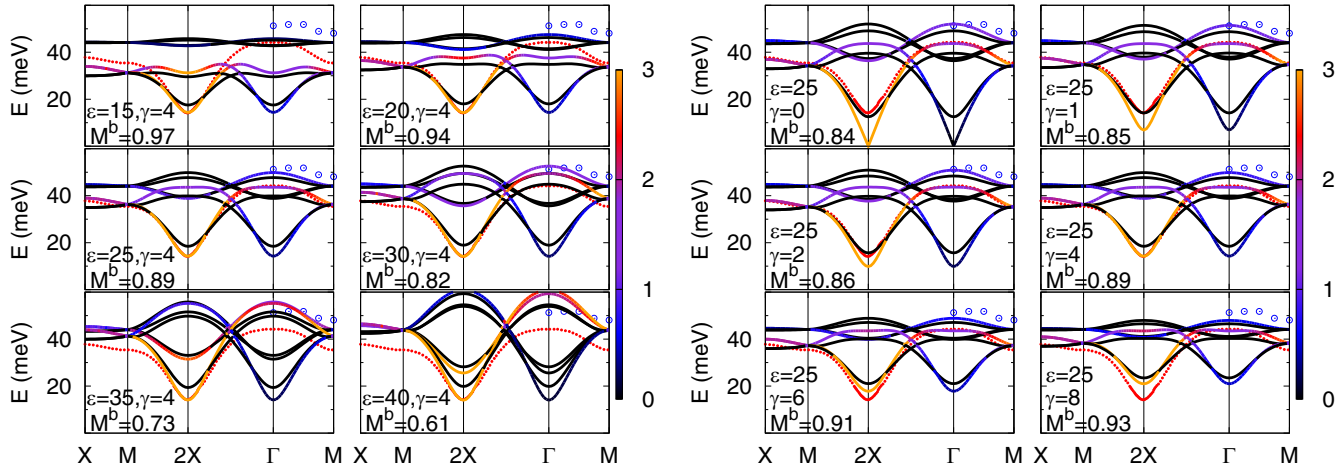

FIG. 5. The magnon dispersion of Ca_2RuO_4 obtained via HCB spin-wave theory. Dots: Experimental points showing the maximum of intensity, taken from Fig. 2(a) in Ref. [3]. Empty circles: Experimental longitudinal modes, taken from Fig. 2(c) in Ref. [3]. Line: Theory. For each considered parameter choice, the associated ordered magnetic moments along the **b** axis, M^b, is specified in the figure. Magnetic configuration: A-centered. Left panels: Effect of varying ε for constant γ. Right panels: Effect of varying γ for constant ε. Special points: $X = (\pi, 0, 0)$, $M = (\pi, \pi, 0)$, $2X = (2\pi, 0, 0)$, $\Gamma = (0, 0, 0)$. The mode intensity scale is given on the right of each panel.

methods give qualitatively similar but not identical spectra; to reproduce the experiments with comparable accuracy, in HCB spin-wave theory a larger in-plane anisotropy γ is needed, due to the different treatment of the zero-field term. To better disentangle the effects of ε and γ, in the left panels of Figs. 4 and 5 we fix γ and vary ε, and do the opposite in the right panels. In the case relevant here, $\gamma \ll \varepsilon, \Gamma_{\mathbf{0}}$. In this regime, increasing ε while keeping all the rest fixed has the main effect of increasing the spin-wave bandwidth. Increasing γ for fixed ε instead opens a gap, which increases with γ, faster in HP than in HCB spin-wave theory.

The spectra displayed in Figs. 4 and 5 evidence two points. The first is that the value of small parameters, which eventually determine γ, are difficult to extract from experimental data with high accuracy, since they depend on a number of theoretical assumptions (e.g., a small neglected term in the Hamiltonian or the approximations implicit in spin-wave theory), in addition to experimental uncertainties or complications. For instance, in the presence of oxygen excess, or when Ru is partially replaced by Ti, magnetic moments can arrange in the B-type configuration; for the latter, the theoretical spin-wave bands are narrower, everything else staying the same. The second (and most important) point is that, despite these uncertainties, the pseudo-Goldstone modes are qualitatively very well reproduced with parameters close to those we obtain theoretically within the *xy*-like orbital ordering picture. Optimal parameters are $\varepsilon \sim 25$ meV, with γ between 0.5 and 1.2 meV for HP spin waves or $\gamma \sim 4$ meV for HCB spin waves—values all within the interval of variation theoretically predicted.

We now turn to analyze the longitudinal modes, using the same parameters. In Fig. 6, we split the total intensity into its transverse components, $I^a(\mathbf{q})$ and $I^c(\mathbf{q})$, and its longitudinal component, $I^b(\mathbf{q})$; the easy axis here is **b**. We find longitudinal modes in the energy interval (40,50) meV, as shown in the right panel of the figure; this is also the energy window in which the putative Higgs mode was reported [3] (circles). The figure shows that the intensity $I^b(\mathbf{q}) \ll I^a(2X)$, in line with the fact that the mode is difficult to detect; still, in our calculation, $I^b(\mathbf{q})$ is comparable to $I^c(\mathbf{q})$, and with the intensity of back-folded modes. An intrinsic longitudinal Higgs-like mode at $\omega \sim 50$ meV thus appears compatible with *xy*-like orbital ordering, if experimentally observable despite the low intensity; small discrepancies in intensity dispersion are reasonable given theoretical assumption (e.g., decay processes are here neglected), experimental uncertainties and the

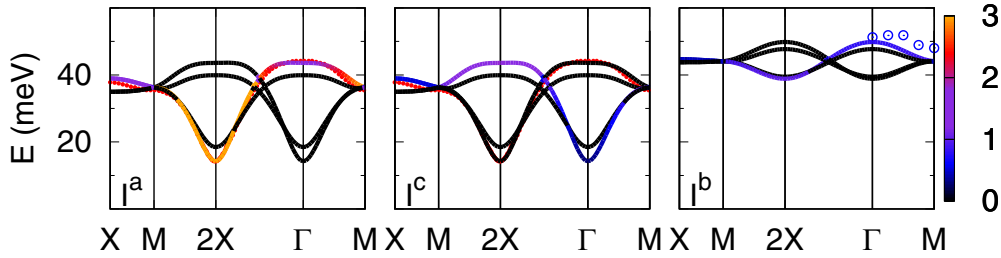

FIG. 6. Magnon dispersion (HCB spin-wave theory) for the A-type magnetic configuration. Dots: Experimental points corresponding to maximum of intensity (from Fig. 2(a) in Ref. [3]). Empty circles: Experimental longitudinal modes (from Fig. 2(c) in Ref. [3]). Lines: Theory ($\varepsilon = 25$ meV, $\gamma = 4$ meV). Special points: $X = (\pi, 0, 0)$, $2X = (2\pi, 0, 0)$, $M = (\pi, \pi, 0)$, $\Gamma = (0, 0, 0)$. The mode intensity scale is given on the right.

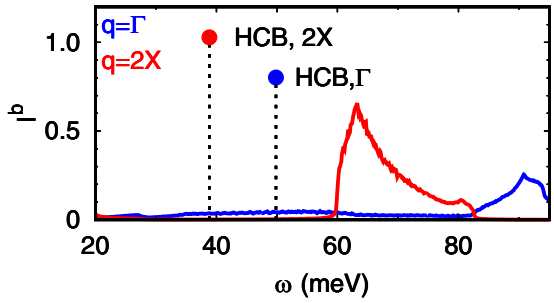

FIG. 7. Ca_2RuO_4: Normalized magnetic intensity of two-magnon longitudinal fluctuation $I^b(\mathbf{q})$ at the ferro- ($\mathbf{q} = \Gamma$) and antiferromagnetic zone center ($\mathbf{q} = 2X$). Parameters: $\varepsilon = 25$ meV and $\gamma = 0.5$ meV, HP spin-wave theory. The results from HCB spin-wave theory ($\varepsilon = 25$ meV, $\gamma = 4$ meV) at representative $\mathbf{q}$ points is shown for comparison. Full lines: A-centered magnetic configuration.

weakness of the signal discussed above. In view of the latter, it is interesting to compare the relative intensity of the intrinsic longitudinal mode with the one associated with longitudinal two-magnon excitations. This is done in Fig. 7; due to the large gap and energy of the longitudinal mode, we neglect here absorption processes. The figure shows that the maximum relative two-magnon intensity is comparable with that of the intrinsic longitudinal mode, but at $\omega \sim 50$ meV appears lower in comparison.

IV. CONCLUSION

We have studied the stability of xy-orbital ordering and the origin of the longitudinal magnetic excitations in Ca_2RuO_4. To this end, we employed a combination of LDA + DMFT calculations and many-body perturbation theory. We have shown that the realization of the nonperturbative spin-orbit regime requires that the crystal-field splitting is reduced to about one-half the LDA value, everything else staying the same. This is a sizable reduction. We therefore confirm that the xy-like orbitally ordered ground state is robust in Ca_2RuO_4. Furthermore, we obtain xy-like orbital ordering also in the much less distorted S-$Pbca$ phase of $Ca_{2-x}Sr_xRuO_4$ with $0 < x < 0.2$ and in the recently identified S^* phase. It would be very interesting to explore if further reduction of local distortion, sufficient to enter the nonperturbative spin-orbit regime, can be achieved via novel chemical engineering, e.g., by replacing partially Ca with other ions such as rare earths [35] or Ba, perhaps in combination with strain [27,35].

Although in Ca_2RuO_4 the spin-orbit interaction can be treated as a perturbation, its effects are nevertheless crucial for describing the spin-wave spectra, since it yields anisotropic spin-interaction terms. In the xy-like orbital ordering regime, magnetism can be described by a minimal effective $S = 1$ spin model with zero-field-splitting. Within experimental and theoretical error bars, this model describes well the transverse pseudo-Goldstone modes. By using HCB spin-wave theory, we show that, in addition, it yields a longitudinal amplitude mode at ∼50 meV. Its intensity is very weak compared to the lowest energy transverse modes, but it appears larger than the one associated with the two-magnon process at the same energy—in the limit in which magnon-magnon scattering and decaying processes can be neglected. While additional experiments would be desirable for the final conclusion, our results indicate that an intrinsic Higgs-like amplitude mode at $\omega \sim 50$ meV with very weak intensity is compatible with xy-like orbital ordering.

ACKNOWLEDGMENTS

G.Z. acknowledges financial support by the National Natural Science Foundation of China under Grant No. 11774349. The authors gratefully acknowledge the Gauss Centre for Supercomputing e.V. (Ref. [36]) for funding this project by providing computing time on the GCS Supercomputer JUWELS at Jülich Supercomputing Centre (JSC).

APPENDIX A: HARD-CORE BOSON SPIN-WAVE THEORY

Here we describe HCB spin-wave theory [24] extended to the case of Ca_2RuO_4. The single-ion tensor in Hamiltonian Eq. (4) is described via the two parameters ε and γ as discussed in the main text. The directional bosons are

$$\hat{a}^\dagger_{js;a} = -\frac{1}{\sqrt{2}}(\hat{a}^\dagger_{js;1} - \hat{a}^\dagger_{js;-1}),$$
$$\hat{a}^\dagger_{js;b} = +\frac{i}{\sqrt{2}}(\hat{a}^\dagger_{js;1} + \hat{a}^\dagger_{js;-1}),$$
$$\hat{a}^\dagger_{js;c} = \hat{a}^\dagger_{js;0},$$

with the on-site hard-core constraint

$$\hat{n}_{js} = \sum_{\mu=a,b,c} \hat{a}^\dagger_{js;\mu}\hat{a}_{js;\mu} = 1. \tag{A1}$$

The components of a spin operator are then given by

$$S_{js;\mu} = -i \sum_{\nu,\xi=a,b,c} \epsilon_{\mu\nu\xi}\hat{a}^\dagger_{js;\nu}\hat{a}_{js;\xi}.$$

In the following, we assume that $\mathbf{b}$ is the easy axis. The condensate HCB creation operators are defined as

$$\hat{b}^\dagger_{js;0} = u\sigma_s\hat{a}^\dagger_{js;c} - iv\hat{a}^\dagger_{js;a}.$$

Here u and v are real numbers and $u^2 + v^2 = 1$; for convenience, we set $u = \sqrt{(1-r)/2}$ and $v = \sqrt{(1+r)/2}$. The integers $\{\sigma_s\}$ specify the collinear magnetic order inside the cell; in the case of Ca_2RuO_4, we have $\{\sigma_s\} = \{1, -1, -1, 1\}$ for the so-called A-centered configuration and $\{\sigma_s\} = \{1, 1, -1, -1\}$ for the B-centered configuration. The orthonormal HCBs describing longitudinal (along the $\mathbf{b}$ axis) spin fluctuations are then

$$\hat{b}^\dagger_{js;L} = u\sigma_s\hat{a}^\dagger_{js;a} - iv\hat{a}^\dagger_{js;c},$$

while

$$\hat{b}^\dagger_{js;T} = \hat{a}^\dagger_{js;b}$$

are the operators for transverse hard-core modes, i.e., for spin fluctuations perpendicular to the direction of the ordered moment. Next we introduce the Fourier transform

$$\Gamma^{s,s'}_{\mathbf{k}} = \frac{1}{2}\sum_{j>0} \Gamma_{0s;js'} e^{i\mathbf{k}\cdot(\mathbf{R}_{js'} - \mathbf{R}_{0s})},$$

where $\mathbf{R}_{js}$ are Ru atom position vectors. Its site-weighted average is $\Gamma_{\mathbf{k}} = -\sum_s \Gamma^{1,s}_{\mathbf{k}} \sigma_1 \sigma_s$ and it is positive for antiferromagnetic couplings. The constraint that the classical ground state minimizes the energy yields $r = (\epsilon - \gamma)/4\Gamma_{\mathbf{0}}$, so $M^b = |\langle S_{js;b} \rangle| = \sqrt{1 - r^2}$. Keeping up to quadratic terms in the $\hat{b}$ HCBs, the spin Hamiltonian can be rewritten as

$$\mathcal{H} = \sum_{\mathbf{k}mss'} \Bigg[\varepsilon^{s,s'}_{\mathbf{k}m} \hat{b}^\dagger_{\mathbf{k}s;m} \hat{b}_{\mathbf{k}s';m} - \frac{1}{2} \Delta^{s,s'}_{\mathbf{k}m} \left(\hat{b}^\dagger_{\mathbf{k}s;m} \hat{b}^\dagger_{-\mathbf{k}s';m} + \hat{b}_{\mathbf{k}s;m} \hat{b}_{-\mathbf{k}s';m} \right) \Bigg], \quad \text{(A2)}$$

where $m = L, T$ and

$$\varepsilon^{s,s'}_{\mathbf{k}L} = 2r^2 \Gamma^{s,s'}_{\mathbf{k}} + 4\Gamma_{\mathbf{0}} \delta_{s,s'},$$
$$\Delta^{s,s'}_{\mathbf{k}L} = 2r^2 \Gamma^{s,s'}_{\mathbf{k}},$$

while

$$\varepsilon^{s,s'}_{\mathbf{k}T} = ((1 + \sigma_s \sigma_{s'}) + r(\sigma_s \sigma_{s'} - 1)) \Gamma^{s,s'}_{\mathbf{k}} + \left(2\Gamma_{\mathbf{0}} + \frac{\epsilon + \gamma}{2} \right) \delta_{s,s'},$$
$$\Delta^{s,s'}_{\mathbf{k}T} = ((\sigma_s \sigma_{s'} - 1) + r(1 + \sigma_s \sigma_{s'})) \Gamma^{s,s'}_{\mathbf{k}}. \quad \text{(A3)}$$

This Hamiltonian can be diagonalized to obtain the spin-wave dispersion $\omega^m_{\mathbf{k},s}$ $(s = 1, .., N_s)$ using the Bogoliubov transformation matrix,

$$\begin{pmatrix} \hat{b}_{\mathbf{k}1,m} \\ \cdot \\ \cdot \\ \hat{b}_{\mathbf{k}N_s,m} \\ \hat{b}^\dagger_{-\mathbf{k}1,m} \\ \cdot \\ \cdot \\ \hat{b}^\dagger_{-\mathbf{k}N_s,m} \end{pmatrix} = \begin{pmatrix} T^{\mathbf{k},m}_{11} & \cdot & \cdot & \cdot & \cdot & \cdot & \cdot & T^{\mathbf{k},m}_{1,2N_s} \\ \cdot & \cdot & \cdot & \cdot & \cdot & \cdot & \cdot & \cdot \\ \cdot & \cdot & \cdot & \cdot & \cdot & \cdot & \cdot & \cdot \\ \cdot & \cdot & \cdot & \cdot & \cdot & \cdot & \cdot & \cdot \\ \cdot & \cdot & \cdot & \cdot & \cdot & \cdot & \cdot & \cdot \\ \cdot & \cdot & \cdot & \cdot & \cdot & \cdot & \cdot & \cdot \\ \cdot & \cdot & \cdot & \cdot & \cdot & \cdot & \cdot & \cdot \\ T^{\mathbf{k},m}_{2N_s,1} & \cdot & \cdot & \cdot & \cdot & \cdot & \cdot & T^{\mathbf{k},m}_{2N_s,2N_s} \end{pmatrix} \begin{pmatrix} \hat{\beta}_{\mathbf{k}1,m} \\ \cdot \\ \cdot \\ \hat{\beta}_{\mathbf{k}N_s,m} \\ \hat{\beta}^\dagger_{-\mathbf{k}1,m} \\ \cdot \\ \cdot \\ \hat{\beta}^\dagger_{-\mathbf{k}N_s,m} \end{pmatrix},$$

where N_s is the number of magnetic ions in the magnetic unit cell. The $\hat{T}$ matrices yield the magnetic intensities:

$$I^b_{p,L}(\mathbf{q}) = r^2 \left| \sum_{s,s'} \mathrm{Re} F^{bL}_{ss';p}(\mathbf{q}) \right|,$$
$$I^c_{p,T}(\mathbf{q}) = \frac{1 - r}{2} \left| \sum_{s,s'} \mathrm{Re} F^{cT}_{ss';p}(\mathbf{q}) \right|,$$
$$I^a_{p,T}(\mathbf{q}) = \frac{1 + r}{2} \left| \sum_{s,s'} \sigma_s \sigma_{s'} \mathrm{Re} F^{aT}_{ss';p}(\mathbf{q}) \right|.$$

The matrices on the right-hand side are defined as

$$F^{dm}_{ss';p}(\mathbf{q}) = T^{\mathbf{q},m}_{N_s+s,p} \overline{T^{\mathbf{q},m}_{N_s+s',p}} + T^{\mathbf{q},m}_{s,p} \overline{T^{\mathbf{q},m}_{s',p}} + \alpha_d T^{\mathbf{q},m}_{N_s+s,p} \overline{T^{\mathbf{q},m}_{s',p}} + \alpha_d T^{\mathbf{q},m}_{s,p} \overline{T^{\mathbf{q},m}_{N_s+s',p}},$$

where $\alpha_d = -1$ for $d = b, a$ and $\alpha_d = 1$ for $d = c$.

For $\varepsilon = \gamma = 0$, the parameter $r = 0$ and the transverse modes are the same as in HP spin-wave theory; furthermore, when $\varepsilon = \gamma$ the longitudinal mode has $\mathbf{k}$-independent energy. The principal difference with respect to HP spin-wave theory, besides the inclusion of longitudinal amplitude modes, is that the effects of the zero-field splitting are treated under the hard-core constraint Eq. (A1).

APPENDIX B: LONGITUDINAL TWO-MAGNON FLUCTUATIONS

Here we calculate the magnetic intensities based on the HP transformation. If $\mathbf{b}$ is the magnetization axis, we have

$$S^b_{js} = \sigma_s (S - \hat{b}^\dagger_{js} \hat{b}_{js}),$$
$$S^c_{js} = \frac{\sqrt{2S}}{2} \left[\left(\sqrt{1 - \frac{\hat{b}^\dagger_{js} \hat{b}_{js}}{2S}} \right) \hat{b}_{js} + \hat{b}^\dagger_{js} \left(\sqrt{1 - \frac{\hat{b}^\dagger_{js} \hat{b}_{js}}{2S}} \right) \right] \approx \frac{\sqrt{2S}}{2} (\hat{b}_{js} + \hat{b}^\dagger_{js}),$$
$$S^a_{js} = \sigma_s \frac{\sqrt{2S}}{2i} \left[\left(\sqrt{1 - \frac{\hat{b}^\dagger_{js} \hat{b}_{js}}{2S}} \right) \hat{b}_{js} - \hat{b}^\dagger_{js} \left(\sqrt{1 - \frac{\hat{b}^\dagger_{js} \hat{b}_{js}}{2S}} \right) \right] \approx \sigma_s \frac{\sqrt{2S}}{2i} (\hat{b}_{js} - \hat{b}^\dagger_{js}).$$

Keeping up to quadratic terms, Hamiltonian Eq. (4) becomes, after subtracting the energy of the ground state,

$$\mathcal{H} = \sum_{\mathbf{k}s,s'} \left[\varepsilon^{s,s'}_{\mathbf{k}} \hat{b}^\dagger_{\mathbf{k}s} \hat{b}_{\mathbf{k}s'} - \frac{\Delta^{s,s'}_{\mathbf{k}}}{2} (\hat{b}^\dagger_{\mathbf{k}s} \hat{b}^\dagger_{-\mathbf{k}s'} + \hat{b}_{\mathbf{k}s} \hat{b}_{-\mathbf{k}s'}) \right],$$

where

$$\varepsilon^{s,s'}_{\mathbf{k}} = S\big((1 + \sigma_s \sigma_{s'}) \Gamma^{s,s'}_{\mathbf{k}} + (2\Gamma_{\mathbf{0}} + \epsilon + \gamma) \delta_{s,s'}\big),$$
$$\Delta^{s,s'}_{\mathbf{k}} = S\big((\sigma_s \sigma_{s'} - 1) \Gamma^{s,s'}_{\mathbf{k}} - 4r\Gamma_{\mathbf{0}} \delta_{s,s'}\big). \quad \text{(B1)}$$

We can obtain the spin-wave dispersion $\omega_{\mathbf{k},s}$ $(s = 1, .., N_s)$ via Bogoliubov transformation. The transformation matrix $\hat{T}$ yields the transverse intensities:

$$I^a_{p,T}(\mathbf{q}) = \frac{S}{2} \left| \sum_{s,s'} \sigma_s \sigma_{s'} \mathrm{Re} F^a_{ss';p}(\mathbf{q}) \right|,$$
$$I^c_{p,T}(\mathbf{q}) = \frac{S}{2} \left| \sum_{s,s'} \mathrm{Re} F^c_{ss';p}(\mathbf{q}) \right|.$$

The (relative) longitudinal two-magnon fluctuations intensity can be then defined as the $\mathbf{k}$ average,

$$I^b(\mathbf{q}, \omega) = \left\langle \left| \sum_{s,s'} \sigma_s \sigma_{s'} \mathrm{Re} F^{p,p';+}_{s,s'}(\mathbf{k}; \mathbf{q}) \right| \right\rangle_{\mathbf{k}},$$

where

$$\langle X(\mathbf{k}; \mathbf{q}) \rangle_{\mathbf{k}} = \frac{\sum_{\mathbf{k}} \sum^{N_s}_{p,p'} X(\mathbf{k}, \mathbf{q}) \delta(\omega - E_{\mathbf{k},p} - E_{\mathbf{k}+\mathbf{q},p'})}{\sum_{\mathbf{k}} \sum^{N_s}_{p,p'} \delta(\omega - E_{\mathbf{k},p} - E_{\mathbf{k}+\mathbf{q},p'})}.$$

The F functions are defined as

$$F^d_{ss';p}(\mathbf{q}) = T^{\mathbf{q}}_{N_s+s,p} \overline{T^{\mathbf{q}}_{N_s+s',p}} + T^{\mathbf{q}}_{s,p} \overline{T^{\mathbf{q}}_{s',p}} + \alpha_d T^{\mathbf{q}}_{N_s+s,p} \overline{T^{\mathbf{q}}_{s',p}} + \alpha_d T^{\mathbf{q}}_{s,p} \overline{T^{\mathbf{q}}_{N_s+s',p}},$$
$$F^{p,p';+}_{s,s'}(\mathbf{k}; \mathbf{q}) = T^{\mathbf{k}}_{s',N_s+p} \overline{T^{\mathbf{k}}_{s,N_s+p}} T^{\mathbf{k}+\mathbf{q}}_{s,p'} \overline{T^{\mathbf{k}+\mathbf{q}}_{s',p'}} + T^{\mathbf{k}}_{N_s+s',N_s+p} \overline{T^{\mathbf{k}}_{s,N_s+p}} T^{\mathbf{k}+\mathbf{q}}_{s,p'} \overline{T^{\prime\mathbf{k}+\mathbf{q}}_{N_s+s',p'}}.$$

[1] S. Kunkemöller, D. Khomskii, P. Steffens, A. Piovano, A. A. Nugroho, and M. Braden, Phys. Rev. Lett. **115**, 247201 (2015). Due to twinning, (100)/(010) directions cannot be distinguished in the experiments.

[2] S. Kunkemöller, E. Komleva, S. V. Streltsov, S. Hoffmann, D. I. Khomskii, P. Steffens, Y. Sidis, K. Schmalzl, and M. Braden, Phys. Rev. B **95**, 214408 (2017).

[3] A. Jain, M. Krautloher, J. Porras, G. H. Ryu, D. P. Chen, D. L. Abernathy, J. T. Park, A. Ivanov, J. Chaloupka, G. Khaliullin, B. Keimer, and B. J. Kim, Nat. Phys. **13**, 633 (2017).

[4] S.-M. Souliou, J. Chaloupka, G. Khaliullin, G. Ryu, A. Jain, B. J. Kim, M. Le Tacon, and B. Keimer, Phys. Rev. Lett. **119**, 067201 (2017).

[5] E. Gorelov, M. Karolak, T. O. Wehling, F. Lechermann, A. I. Lichtenstein, and E. Pavarini, Phys. Rev. Lett. **104**, 226401 (2010).

[6] G. Zhang and E. Pavarini, Phys. Rev. B **95**, 075145 (2017). Here the adopted enhancement is $\lambda_{\rm eff}/\lambda \sim 1.8/\sqrt{2}$.

[7] G. Zhang and E. Pavarini, Phys. Status Solidi RRL **12**, 1800211 (2018).

[8] D. G. Porter, V. Granata, F. Forte, S. Di Matteo, M. Cuoco, R. Fittipaldi, A. Vecchione, and A. Bombardi, Phys. Rev. B **98**, 125142 (2018).

[9] H. Gretarsson, H. Suzuki, Hoon Kim, K. Ueda, M. Krautloher, B. J. Kim, H. Yavaş, G. Khaliullin, and B. Keimer, Phys. Rev. B **100**, 045123 (2019).

[10] G. Cao, S. McCall, M. Shepard, J. E. Crow, and R. P. Guertin, Phys. Rev. B **56**, R2916(R) (1997).

[11] C. S. Alexander, G. Cao, V. Dobrosavljevic, S. McCall, J. E. Crow, E. Lochner, and R. P. Guertin, Phys. Rev. B **60**, R8422(R) (1999).

[12] M. Braden, G. André, S. Nakatsuji, and Y. Maeno, Phys. Rev. B **58**, 847 (1998).

[13] G. Cao, S. McCall, V. Dobrosavljevic, C. S. Alexander, J. E. Crow, and R. P. Guertin, Phys. Rev. B **61**, R5053(R) (2000).

[14] O. Friedt, M. Braden, G. André, P. Adelmann, S. Nakatsuji, and Y. Maeno, Phys. Rev. B **63**, 174432 (2001).

[15] G. Khaliullin, Phys. Rev. Lett. **111**, 197201 (2013).

[16] A. Akbari and G. Khaliullin, Phys. Rev. B **90**, 035137 (2014).

[17] The atomic t_{2g} multiplet with $J_{\rm tot} = 0$ can be expressed as follows:

$$|0\rangle = \frac{1}{\sqrt{3}}\Big[|xy,0\rangle - \frac{i}{\sqrt{2}}[|xz,-1\rangle + i|yz,-1\rangle] - \frac{i}{\sqrt{2}}[|xz,+1\rangle - i|yz,+1\rangle]\Big],$$

where $|xy,0\rangle = \frac{1}{\sqrt{2}}\sum_\sigma c^\dagger_{yz,-\sigma}c^\dagger_{xz\sigma}c^\dagger_{xy\uparrow}c^\dagger_{xy\downarrow}|0\rangle$, $|xz,2\sigma\rangle = c^\dagger_{yz\sigma}c^\dagger_{xy\sigma}c^\dagger_{xz\uparrow}c^\dagger_{xz\downarrow}|0\rangle$, and $|yz,2\sigma\rangle = c^\dagger_{xz\sigma}c^\dagger_{xy\sigma}c^\dagger_{yz\uparrow}c^\dagger_{yz\downarrow}|0\rangle$.

[18] I. Zegkinoglou, J. Strempfer, C. S. Nelson, J. P. Hill, J. Chakhalian, C. Bernhard, J. C. Lang, G. Srajer, H. Fukazawa, S. Nakatsuji, Y. Maeno, and B. Keimer, Phys. Rev. Lett. **95**, 136401 (2005).

[19] M. Rams, M. Krůzel, A. Zarzycki, K. Krolas, and K. Tomala, Phy. Rev. B **80**, 045119 (2009).

[20] J. H. Jung, Z. Fang, J. P. He, Y. Kaneko, Y. Okimoto, and Y. Tokura, Phys. Rev. Lett. **91**, 056403 (2003).

[21] D. Sutter, C. G. Fatuzzo, S. Moser, M. Kim, R. Fittipaldi, A. Vecchione, V. Granata, Y. Sassa, F. Cossalter, G. Gatti, M. Grioni, H. M. Rønnow, N. C. Plumb, C. E. Matt, M. Shi, M. Hoesch, T. K. Kim, T.-R. Chang, H.-T. Jeng, C. Jozwiak, A. Bostwick, E. Rotenberg, A. Georges, T. Neupert, and J. Chang, Nat. Commun. **8**, 15176 (2017).

[22] H. Liu and G. Khaliullin, Phys. Rev. Lett. **122**, 057203 (2019).

[23] J. Bertinshaw, N. Gurung, P. Jorba, H. Liu, M. Schmid, D. T. Mantadakis, M. Daghofer, M. Krautloher, A. Jain, G. H. Ryu, O. Fabelo, P. Hansmann, G. Khaliullin, C. Pfleiderer, B. Keimer, and B. J. Kim, Phys. Rev. Lett. **123**, 137204 (2019).

[24] M. Matsumoto and M. Koga, J. Phys. Soc. Jpn. **76**, 073709 (2007).

[25] For a pedagogical presentation see, e.g., E. Pavarini, The LDA+DMFT Approach, in *The LDA+DMFT Approach to Strongly Correlated Materials*, edited by E. Pavarini, E. Koch, D. Vollhardt, and A. Lichtenstein, Modeling and Simulation, Vol. 1 (Forschungszentrum Jülich, Jülich, 2011), http://www.cond-mat.de/events/correl11/manuscripts/pavarini.pdf.

[26] J. Mravlje, M. Aichhorn, T. Miyake, K. Haule, G. Kotliar, and A. Georges, Phys. Rev. Lett. **106**, 096401 (2011).

[27] C. Dietl. S. K. Sinha, G. Christiani, Y. Khaydukov, T. Keller, D. Putzky, S. Ibrahimkutty, P. Wochner, G. Logvenov, P. A. van Aken, B. J. Kin, and B. Keimer, Appl. Phys. Lett. **112**, 031902 (2018).

[28] From the relative extension of the Wannier functions, $U_{xz,xz} > U_{xy,xy}$ and $U_{yz,yz} > U_{xy,xy}$. This further stabilizes xy orbital ordering, i.e., it enhances the effects of the crystal-field splitting. If, instead, screening effects were much more efficient for the xz/yz orbitals, the opposite would be true. Here, for simplicity, we only consider the essential parameter for studying the stability of xy orbital ordering, the effective crystal-field splitting.

[29] P. Steffens, O. Friedt, P. Alireza, W. G. Marshall, W. Schmidt, F. Nakamura, S. Nakatsuji, Y. Maeno, R. Lengsdorf, M. M. Abd-Elmeguid, and M. Braden, Phys. Rev. B **72**, 094104 (2005).

[30] Z. V. Pchelkina, I. A. Nekrasov, Th. Pruschke, A. Sekiyama, S. Suga, V. I. Anisimov, and D. Vollhardt, Phys. Rev. B **75**, 035122 (2007).

[31] G. Zhang, E. Gorelov, E. Sarvestani, and E. Pavarini, Phys. Rev. Lett. **116**, 106402 (2016).

[32] M. Kim, J. Mravlje, M. Ferrero, O. Parcollet, and A. Georges, Phys. Rev. Lett. **120**, 126401 (2018).

[33] G. Zhang and E. Pavarini, Phys. Rev. B **99**, 125102 (2019).

[34] A. Tamai, M. Zingl, E. Rozbicki, E. Cappelli, S. Riccò, A. de la Torre, S. McKeown Walker, F. Y. Bruno, P. D. C. King, W. Meevasana, M. Shi, M. Radović, N. C. Plumb, A. S. Gibbs, A. P. Mackenzie, C. Berthod, H. U. R. Strand, M. Kim, A. Georges, and F. Baumberger, Phys. Rev. X **9**, 021048 (2019).

[35] S. Riccò, M. Kim, A. Tamai, S. McKeown Walker, F. Y. Bruno, I. Cucchi, E. Cappelli, C. Besnard, T. K. Kim, P. Dudin, M. Hoesch, M. J. Gutmann, A. Georges, R. S. Perry, and F. Baumberger, Nat. Comm. **9**, 4535 (2018).

[36] www.gauss-centre.eu